The 5d-5p-3d orbital hybridization induced by light incorporation of Cu into surface-uneven Pt_3Sn intermetallic nanocubes customizes dual-intermediates adsorptions for CO-resilient methanol oxidation

Yao Nie [a],[*], Zhaohong Li [a], Yi Wang [a], Xingqun Zheng [b],[*], Linping Luo [a], Xuejiao Xia [a], Sitong Yang [a], Chunyan Du [a], Yihan Huang [a], Yi Wang [a],[*]

[a] *Chongqing Key Laboratory of Green Synthesis and Applications, College of Chemistry, Chongqing Normal University, Chongqing 401331, China*
[b] *College of Safety Engineering, Chongqing University of Science & Technology, Chongqing 401331, China*

ARTICLE INFO

ABSTRACT

Catalysts with excellent performances for methanol oxidation reaction (MOR) are supposed to equip with a weaker *CO adsorption but a stronger *OH adsorption. Herein, light incorporation of Cu is implemented into surface-uneven Pt_3Sn intermetallic nanocubes to manipulate crucial CO*/OH* intermediates adsorptions for boosting MOR electrocatalysis. The generated ternary $Cu_{0.2}Pt_3Sn$/CNTs intermetallic preserves the uneven cubic shape of non-doped Pt_3Sn/CNTs, providing a defect-rich surface structure for affording abundant available active sites. More importantly, the incorporated Cu induces a strong Pt 5d-Sn 5p-Cu 3d orbital hybridization, which upgrades the electron density of Pt but reversely downgrades that of Sn. Such delicately tailored local coordination environments of Pt and Sn result in an intrinsically attenuated CO* adsorption on Pt sites but a promoted OH* adsorption on Sn sites, remarkably diminishing the energy barrier of CO* oxidation. The elaborately customized dual-intermediates adsorptions combined with the defect-rich cubic architecture superiorities consequently contribute to highly elevated MOR performance.

1. Introduction

The electro-oxidation of methyl alcohol plays an important role in the low-temperature proton exchange membrane fuel cells, bio-mass conversion and fine chemistry [1,2]. However, the methanol oxidation reaction (MOR) involving multi-proton coupled six-electron transfer process suffers from notoriously sluggish kinetics, obstructing rapid developments of relevant devices or technologies [3,4]. Pt is the most active monometallic catalyst for speeding up MOR kinetics in acidic media, unfortunately, its performance is usually stifled by the poisoning issue of toxic CO*, the most stable intermediate produced during MOR [1,5]. The inherently strong chemisorption for CO* and the poor ability in dissociating water to yield oxygenated species (e.g., OH*), jointly lead to huge CO* oxidation barrier on Pt, especially at low overpotential regions [6–8]. Targeting at accelerating the oxidative removal of CO* and enhancing the overall MOR kinetics, tremendous efforts have been thereby devoted to adjusting the CO*/OH* binding energies of Pt. Specifically, it is crucial to selectively weaken the adsorption energy for CO* but strengthen the adsorption energy for OH*. An effective strategy

to realize this is by alloying Pt with oxophilic metals (M), such as Ru, Sn, Fe, Co, Ni, Cu and etc. On these Pt-M catalysts, OH* can be easily adsorbed on M sites at lower potentials than those on Pt, thus triggering the conversion of CO* bonded on nearby Pt sites to CO_2 [9–12]. Meanwhile, the electronic structure of Pt can be modulated by M via the induced strain or ligand effects to enable a downshifted d-band center of Pt, resulting in an intrinsically weakened Pt-CO bonding strength [13–15].

Despite the ameliorated CO-tolerant ability and MOR activity, common Pt-M alloys in the form of disordered solid solutions are often criticized for their poor operation durability as the additional M units easily tend to dealloy under highly corrosive MOR conditions, ultimately leading to disintegration of catalysts [16–19]. In contrast to random alloys, Pt-based intermetallic compounds with atomically ordered arrangements are advantageous in vanquishing dissolution issues due to the higher mixing enthalpy and stronger 3d-5d orbital coupling between Pt and M[20–22]. Moreover, the well-defined coordination environments of intermetallics endow Pt with a much more unique electronic state for optimizing the adsorption energies toward intermediates and

intensifying the catalytic activity [23–26]. Further engineering crystal shapes over Pt-based intermetallic materials could tailor the nature and the number of surface exposed active sites more deeply[27,28], pushing their activity to new levels while simultaneously reserving their merits of high stability due to the combination of the benefits from shaping and atomic ordering. Of various finely shaped Pt-based intermetallic compounds available[29–34], cubic Pt_3Sn intermetallic nanocrystals with a $L1_2$ crystalline phase structure have received special research attention because of its low disordered-to-ordered phase-transition temperature (below 200 °C), easy manufacture (one-step solvothermal synthesis) and adjustable surface structures (varied concavities and surface defect concentrations) [29,35]. Nevertheless, the reported MOR activity of those surface-engineered Pt_3Sn intermetallic nanocrystals has been unsatisfactory[36]. Pioneering studies have disclosed that the robust resistance to be oxidized of Sn sites in highly ordered Pt_3Sn intermetallic materials contrariwise gives rise to a disappointing affinity to OH* [37, 38], making the release of CO*-Pt sites harder due to the loss of timely OH* supplying. Therefore, to fully exploiting the integrated shaping and atomic ordering superiorities of tractable Pt_3Sn intermetallic nanocrystals in MOR electrocatalysis, extra strategies beyond shape and ordered phase engineering are required to further tune their chemisorption properties towards crucial intermediates.

In this work, light doping of Cu is implemented into surface-uneven Pt_3Sn intermetallic nanocubes to manipulate the adsorption energies of key intermediates (CO* and OH*) for advancing the design of MOR electrocatalysts. The yielded tri-intermetallic $Cu_{0.2}Pt_3Sn$ nanocrystals supported on carbon nanotubes (denoted as $Cu_{0.2}Pt_3Sn$/CNTs) inherit the uneven cubic shape and the intermetallic phase of non-doped Pt_3Sn/CNTs counterpart, but exhibit significant enhancements for MOR. Experimental and theoretical results demonstrate that a strong Pt 5d-Sn 5p-Cu 3d orbital hybridization induced by slight Cu heteroatom doping reversely regulates the local electron densities of Pt and Sn atoms, resulting in an intrinsically decreased CO* adsorption on Pt sites but a promoted OH* adsorption on Sn sites. The profoundly optimized CO*/OH* binding energies that originating from the strong trimetallic couplings, combined with the uneven defect-rich cube architecture superiorities that offering rich available active sites, synergistically lead to outstanding MOR kinetics. Besides, the as-fabricated $Cu_{0.2}Pt_3Sn$/CNTs also delivers a robust stability with fewer structural evolutions as benefiting from the atomically ordered intermetallic phase, highlighting its future practical application. To the best of our knowledge, this is the first report for elucidating relationship between phase/surface structures of well-shaped ternary intermetallic materials and MOR properties/performances.

2. Experimental methods

2.1. Materials

Platinum (II) acetylacetonate ($Pt(acac)_2$), Copper (II) acetylacetonate ($Cu(acac)_2$), Tin (II) chloride dehydrate ($SnCl_2·2H_2O$), N,N-Dimethylformamide (DMF), Poly (N-vinyl-2-pyrrolidone) (PVP, M_W=30000) and Nafion (5 wt%) was purchased from Sigma-Aldrich. Sulfuric acid (H_2SO_4), benzoic acid, ethanol, methanol and carbon nanotubes (CNTs, with external diameter of 20–50 nm) were purchased from Adamas-beta. Commercial Pt/C (20 wt%) and PtRu/C (40 wt%) were purchased from American Johnson-Matthey Corporation. Deionized water used in all experiments is ultrapure grade and the resistivity is 18 MΩ·cm^{-1}.

2.2. Catalyst preparation

The synthesis of $Cu_{0.2}Pt_3Sn$/CNTs is modified from the method reported previously[29]. Typically, 80 mg of CNTs powder (pre-treated by concentrated H_2SO_4 and HNO_3), 40.32 mg of $Pt(acac)_2$, 7.82 mg of $SnCl_2·2H_2O$, 9.07 mg of $Cu(acac)_2$ and 328.05 mg of PVP were dissolved

in 20 mL of DMF. Then, the mixture solution was stirred vigorously for 24 h at room temperature, followed by transferred into a 50 mL Teflon-lined stainless-steel autoclave. The autoclave was sealed and maintained at 180 °C for 12 h. The as-prepared black precipitates were centrifuged, washed multiple times with 1:1 ethanol/water. The Pt_3Sn/CNTs counterpart with Pt_3Sn intermetallic nanocubes directly loading on the CNTs was prepared by the similar solvothermal procedure to above except without adding $Cu(acac)_2$.

Pure Pt nanocubes supported on CNTs (Pt_{NC}/CNTs) were also prepared for comparison. In a typical synthesis, 40.3 mg of $Pt(acac)_2$ and 307.4 mg of benzoic acid were dissolved in 32 mL of DMF. Then, the mixture solution was stirred vigorously for 24 h at room temperature, followed by transferred into a 50 mL Teflon-lined stainless-steel autoclave. The autoclave was sealed and maintained at 160 °C for 12 h. The as-prepared black precipitates were centrifuged and washed multiple times with 1:1 ethanol/water.

3. Results and discussions

3.1. Phase composition and structure characterization

The successful synthesis of $Cu_{0.2}Pt_3Sn$/CNTs relies on a modified kinetically controlled solvothermal reaction[29], as illustrated in Fig. 1a. Briefly, a homogeneous solution of $Pt(acac)_2$, $SnCl_2$, $Cu(acac)_2$, PVP and CNTs dissolved in N, N-dimethylformamide (DMF) was heated at 180 °C for 12 h. As a control, binary intermetallic Pt_3Sn supported on CNTs (Pt_3Sn/CNTs) were also successfully synthesized with a similar process of $Cu_{0.2}Pt_3Sn$/CNTs except for without adding of copper precursors. The compositions of as-synthesized $Cu_{0.2}Pt_3Sn$/CNTs and Pt_3Sn/CNTs were measured by inductively coupled plasma atomic emission spectrometry (ICP-AES) (Table S1), which is consistent with theoretical feeding values, revealing the complete reduction of the precursors. The crystalline structures of as-synthesized catalysts were probed by powder X-ray diffraction (XRD) technique. A broad diffraction peak at about 25° for $Cu_{0.2}Pt_3Sn$/CNTs and Pt_3Sn/CNTs displayed in Fig. 1b is assigned to the (002) plane of the CNTs support. Pt_3Sn/CNTs shows the diffraction peaks matching well with the standard card of $L1_2$-type Pt_3Sn (JCPD-65-0958) [35], confirming the successful formation of intermetallic Pt_3Sn crystal structure. With about 0.2 at% of Cu atoms incorporating, the $Cu_{0.2}Pt_3Sn$/CNTs shares almost similar diffraction peaks to Pt_3Sn/CNTs counterpart but shows mildly decreased intensities of the super-lattice (100) and (110) planes (characteristic of the $L1_2$ ordered Pt_3Sn structure, marked by asterisks), indicating that the $Cu_{0.2}Pt_3Sn$/CNTs are still mainly atomically ordered. It is also found that the diffraction peaks of $Cu_{0.2}Pt_3Sn$/CNTs are slightly shifted toward the higher angle with respect to Pt_3Sn/CNTs, suggesting the successful introduction of Cu into the Pt_3Sn lattice with a lattice contraction. The extent of lattice contraction of Pt in $Cu_{0.2}Pt_3Sn$/CNTs relative to that of Pt_3Sn/CNTs counterpart is − 0.43% (Table S2), as calculated based on Debye-Scherrer equation [39,40]. It is noteworthy to mention that excessive adding of Cu would completely destruct the ordered intermetallic phase, as evidenced by the XRD presented in Fig. S1. With Cu concentration increases, the super-lattice reflections of Cu_xPt_3Sn/CNTs catalysts (x represents the atomic ratio of Cu, varying from 0.6 to 1.5) disappear and peaks gradually shift to higher 2θ values, signifying that controlling the Cu doping content at a low level is crucial to maintain the intermetallic phase structure of $L1_2$ Pt_3Sn.

Transmission electron microscopy (TEM) was initially applied to characterize the morphological features of the as-fabricated $Cu_{0.2}Pt_3Sn$/CNTs. TEM image shown in Fig. S2 indicates that $Cu_{0.2}Pt_3Sn$ nanocrystals are well dispersed on the CNTs support. High-resolution TEM image demonstrates that nanocrystals in $Cu_{0.2}Pt_3Sn$/CNTs (Fig. 1c) have a cubic structure with a rough surface structure, and their average edge length is around ~24 nm. Similar to the $Cu_{0.2}Pt_3Sn$/CNTs, the as-synthesized Pt_3Sn nanocrystals in Pt_3Sn/CNTs also possess a surface-uneven cubic morphology (Fig. S3a). Such uneven surfaces implies a
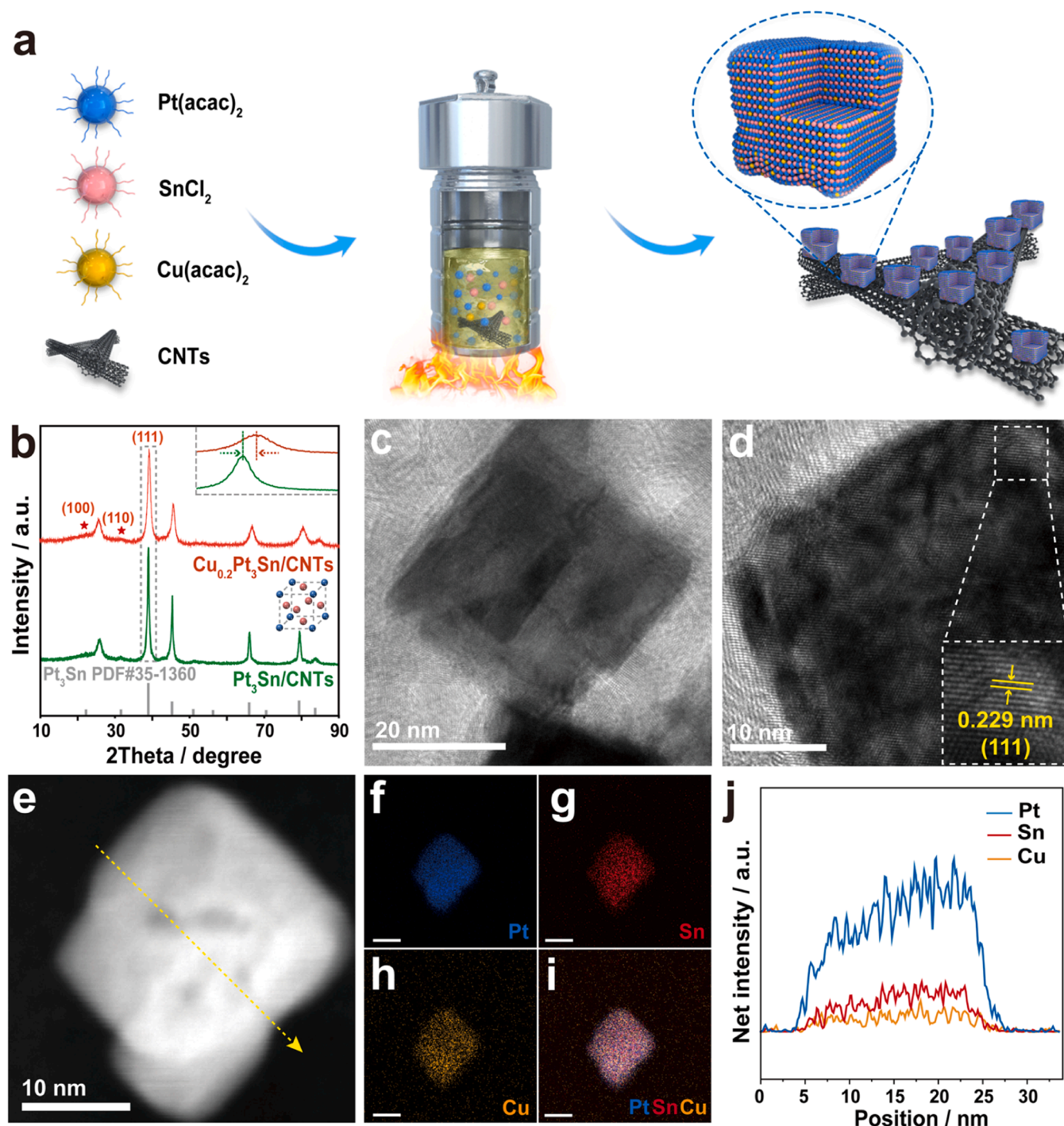
Fig. 1. (a) Schematic illustration of the fabrication of $Cu_{0.2}Pt_3Sn/CNTs$. (b) XRD patterns. (c)-(d) HRTEM image of $Cu_{0.2}Pt_3Sn/CNTs$. (e) HAADF-STEM image of an individual $Cu_{0.2}Pt_3Sn$ nanocubes and (f-i) corresponding EDS elemental mapping. (j) The line-scanning profile of e, along the yellow arrow.

defect-rich characteristic, which would be beneficial to exposing more Pt active sites for enhancing MOR[29,35]. The HRTEM image taken from individual $Cu_{0.2}Pt_3Sn$ particle shows well-defined fringes with the interplanar spacing of 0.229 nm (Fig. 1d), which is assigned to the (111) lattice plane. This spacing value is slightly smaller than the (111) lattice plane of un-doped $Pt_3Sn/CNTs$ (0.231 nm, Fig. S3b, Table S3), confirming again the lattice contraction originating from the incorporation of smaller-radius Cu into Pt_3Sn lattice. The high-angle annular dark-field scanning TEM (HADDF-STEM) and corresponding energy-dispersive spectroscopy (EDS) mapping and line-scan profile presented in Fig. 1e-j verify that the elements of Pt, Sn and Cu are evenly distributed

within the whole nanocubes. Additionally, the Cu/Pt/Sn/ atomic ratio estimated from line-scan profile is 3.08: 1: 0.28, which is almost consistent with the ICP-AES result.

To precisely probe the atomic structure of the $Cu_{0.2}Pt_3Sn/CNTs$, atomic-level analysis was supported by aberration-corrected high-angle annular dark-field scanning transmission electron microscopy (AC-HAADF-STEM). Fig. 2a clearly shows that the $Cu_{0.2}Pt_3Sn$ nanocrystal is not a perfect cube but with many irregular depressions on surface. The high-magnification edge images depict the atomic step structures on the surface, confirming the defect-rich surface feature (Fig. 2b, Fig. S4). The defective surface structure would result in enhanced catalytic
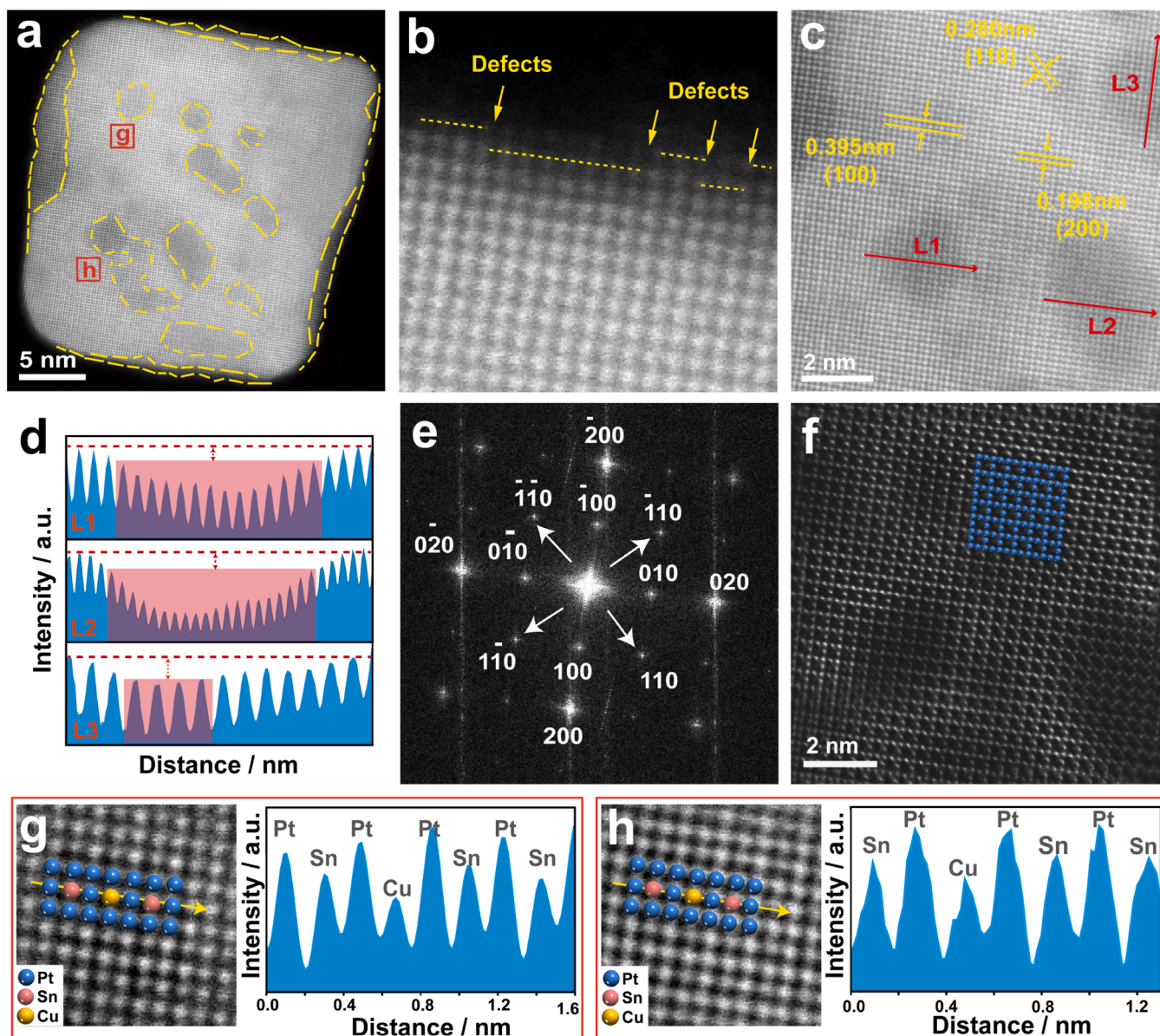
Fig. 2. (a) AC-HAADF-STEM images of $Cu_{0.2}Pt_3Sn/CNTs$. (b)-(c) Enlarged AC-HAADF-STEM images. (d) Intensity profile along the red lines in (c). (e) Fast Fourier transform of (a). (f) Selective inverse Fourier transform of (110) spots from (c). (g)-(h) Magnified AC-HAADF-STEM images (with the overlapping schematics of the Pt/Sn/Cu atoms) of the selected area in (a), and corresponding HAADF line profiles of along the yellow lines.

performance by the generation of abundant active sites[41]. Further through the intensity analysis of the atomic column in the center of the unevenness (L1, L2, and L3 marked in Fig. 2c), it can be seen that middle peaks marked in red are visibly lower than the two sides (Fig. 2d), evidencing again the uneven outline of as-synthesized $Cu_{0.2}Pt_3Sn$ nanocubes[28]. Fig. 2e shows the fast Fourier transform (FFT) of Fig. 2a, the spots from (100) and (110) super-lattice planes along the [001] zone axis are clearly present, reflecting again the ordered characteristic of $Cu_{0.2}Pt_3Sn/CNTs$. Interplanar spacings assigned to be (100), (110) and (200) planes were also measured in Fig. 2c. Noting that the all measured spacing values are slightly smaller than the standard Pt_3Sn intermetallic (Table S3), agreeing well with the XRD patterns of $Cu_{0.2}Pt_3Sn/CNTs$ and further confirming the successful Cu doping. To reflect the atomically ordered characteristic of $Cu_{0.2}Pt_3Sn$ nanocrystals more clearly, inverse Fourier transform by selectively masking the (110) spots in Fig. 2c was conducted. As shown in Fig. 2f, the (110) spots indexed to the ordered domain almost extend across the whole area, indicating the $Cu_{0.2}Pt_3Sn/CNTs$ follows an atomic arrangement corresponding to the

$L1_2$-type Pt_3Sn intermetallic structure. The magnified atom columns combined with the corresponding line intensity profiles (Fig. 2g and h) clearly show the periodic rectangular array of Pt atom columns surrounding the Sn (a lot) and Cu atom (a little) columns, further evidencing the formation of ternary ordered structure of $Cu_{0.2}Pt_3Sn$ with alternately arranged atoms.

X-ray photoelectron spectroscopy (XPS) was investigated to identify the electron structure of the catalysts. The high-resolution XPS spectra of Pt 4 f shown in Fig. 3a reflect that Pt (0) and Pt (II) co-exist in both $Cu_{0.2}Pt_3Sn/CNTs$ and $Pt_3Sn/CNTs$, and most of the surface Pt remains in the metallic state. Fig. 3b shows the deconvoluted Sn 3d spectra of $Cu_{0.2}Pt_3Sn/CNTs$ and $Pt_3Sn/CNTs$, which can be split into three paired peaks ascribed to Sn (0), Sn (II) and Sn (IV) species. The Cu 2p spectra of $Cu_{0.2}Pt_3Sn/CNTs$ presented in Fig. S5 shows a very weak signal since the amount of the Cu dopant on surface is very little. Further analysis points out that the Pt 4 $f_{7/2}$ and Sn $3d_{5/2}$ binding energies of the $Cu_{0.2}Pt_3Sn/CNTs$ are slightly negatively (~0.21 eV) and positively shifted (~0.24 eV), respectively, as compared to those of $Pt_3Sn/CNTs$. Also, the
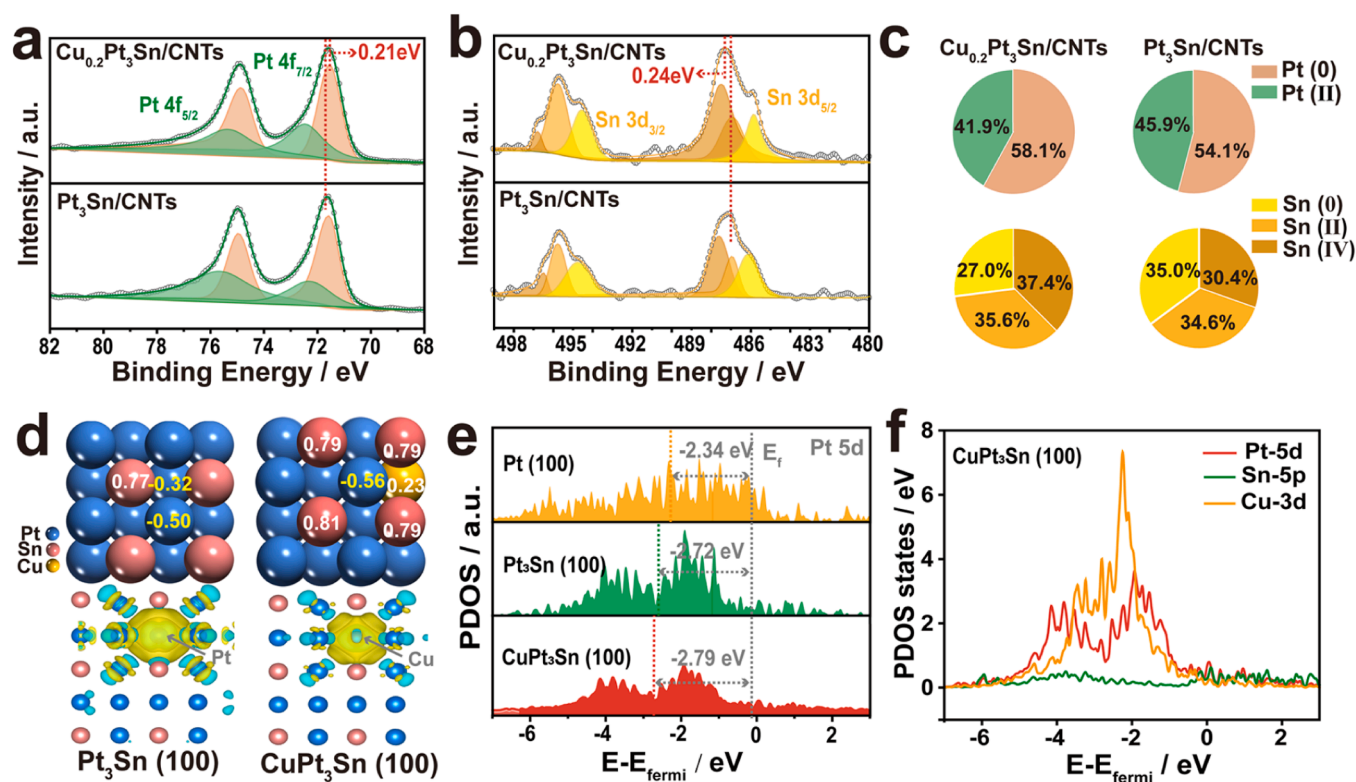
Fig. 3. (a) Pt 4 f XPS spectra and (b) Sn 3d spectra of $Cu_{0.2}Pt_3Sn/CNTs$ and $Pt_3Sn/CNTs$. (c) Atomic ratios of Pt (0), Pt (II), Sn (0) and Sn (II/IV) in $Cu_{0.2}Pt_3Sn/CNTs$ and $Pt_3Sn/CNTs$ obtained from XPS analysis. (d) The Bader charge (top) and the side view of charge density difference (bottom) of Pt_3Sn (100) and $CuPt_3Sn$ (100) models. The yellow and light blue isosurfaces represent charge accumulation and depletion, respectively, with isosurface level set to 0.002e Å^{-3}. (e) The PDOS of surface Pt atoms and d-band center positions of three models. (f) The PDOS of $CuPt_3Sn$ (100) model showing the Pt 5d-orbital, Sn 5p-orbital and Cu 3d-orbital.

Pt (0) and Sn (II/IV) species after Cu doping become more abundant than the Pt (II) and Sn (0) species (Fig. 3c). These changes are inferred to be related to the electronic interaction among Pt, Sn and Cu. The Pt in $Cu_{0.2}Pt_3Sn$ may act as an "electron-acceptor" and the existence of more metallic state of Pt signifies the stronger oxidation resistance [42,43].

The electronic interactions in $Cu_{0.2}Pt_3Sn/CNTs$ were then deeply probed by theoretical modelling. Pt_3Sn (100) and $CuPt_3Sn$ (100) models were established to simulate the catalytic surface of $Pt_3Sn/CNTs$ and $Cu_{0.2}Pt_3Sn/CNTs$, respectively (Fig. S6a, b). The non-alloyed Pt (100) model was also established for comparison (Fig. S6c). Seen from the Bader charge shown in Fig. 3d, the Pt site accumulates negative charges while the neighboring Sn metal site accumulates positive charges, verifying an electron transfer from Sn to Pt, which is consistent with many previous reported Pt_3Sn materials[38,44]. When few Cu atoms incorporate, the surrounding Sn and Pt sites becomes more negative and positive charged, respectively, agreeing well with the binding energy shift results of Pt 4 f and Sn 3d XPS spectra. Meanwhile, an electron donation also occurs from the Cu to the neighboring Pt as the Cu presents a positively charged feature. The charge density difference (Fig. 3d, Fig. S7 and S8) reveals that the Pt atoms nearby the sublayer Cu atom in $CuPt_3Sn$ (100) surface show less electronic depletions (blue regions) than the identical Pt atoms in Pt_3Sn (100) surface, and the electronic accumulation regions (yellow) between Cu and Pt are more closer to Pt atoms, which also indicate an electron transferring from Cu to Pt. From above, it can be preliminarily concluded that Cu doping induces a distinct charge redistribution in $CuPt_3Sn$ (100), and both Cu and Sn furnish electrons to Pt, endowing the Pt atoms locating at $CuPt_3Sn$ (100) surface with an electron-rich feature, corroborating again the XPS result. Further analysis of the plot of projected d-density of states (PDOS) of studied model surfaces illustrates the electronic structure and metal-metal interactions in depth. As seen from the PDOS of Pt-5d orbitals shown in Fig. 3e, the d-band center in Pt_3Sn (100) surface

(−2.72 eV) downward shifts as compared to pure Pt (100) surface (−2.34 eV), which can be ascribed to the coupling between Pt 5d-orbital and Sn 5p-orbital (Fig. S9) and the electron transfer from Sn to Pt. Upon Cu incorporation, an obvious hybridization between Pt 5d-orbital, Sn 5p-orbital and Cu 3d-orbital is observed since the band energy of these three orbitals matches very well, especially in the energy range of − 6 ~0 eV (Fig. 3f). Such a strong 5d-5p-3d orbital hybridization further modulates the electronic structure of $CuPt_3Sn$ (100), narrowing down the Pt d-band width and making the Pt-5d orbital gain more electrons, consequently resulting in a more downshifted d-band center (−2.79 eV). According to the d-band center theory that used to forecast the surface adsorption strength between the metal surface and reaction intermediates, the downshifted d-band center from the Fermi level would weaken the binding strength of intermediate species and thereby accelerate reaction proceedings[9,45–48]. Benefiting from the significantly modulated atomic configuration, strain, ligand environment and electronic states, it is can be reasonably expected that the $Cu_{0.2}Pt_3Sn/CNTs$ catalyst would deliver the enhanced CO tolerance and MOR activity in the following electrochemical tests.

3.2. MOR activity determination

Electrocatalytic performances were evaluated on $Cu_{0.2}Pt_3Sn/CNTs$ and $Pt_3Sn/CNTs$, together with the pure Pt nanocubes supported on CNTs ($Pt_{NC}/CNTs$, Fig. S10) and commercial Pt/C. Cyclic voltammetry (CV) was firstly carried out in N_2-saturated 0.5 M H_2SO_4 to activate and clean the electrocatalysts. Fig. 4a shows the representative stable CV curves of four electrocatalysts and all of them display the well-defined peaks assigned to hydrogen adsorption/desorption. The electrochemical surface area (ECSA) of them was calculated by both integrating the charge from the hydrogen adsorption/desorption (ECSA-H) and CO stripping (ECSA-CO, the CO stripping curves are shown in Fig. 4g, which
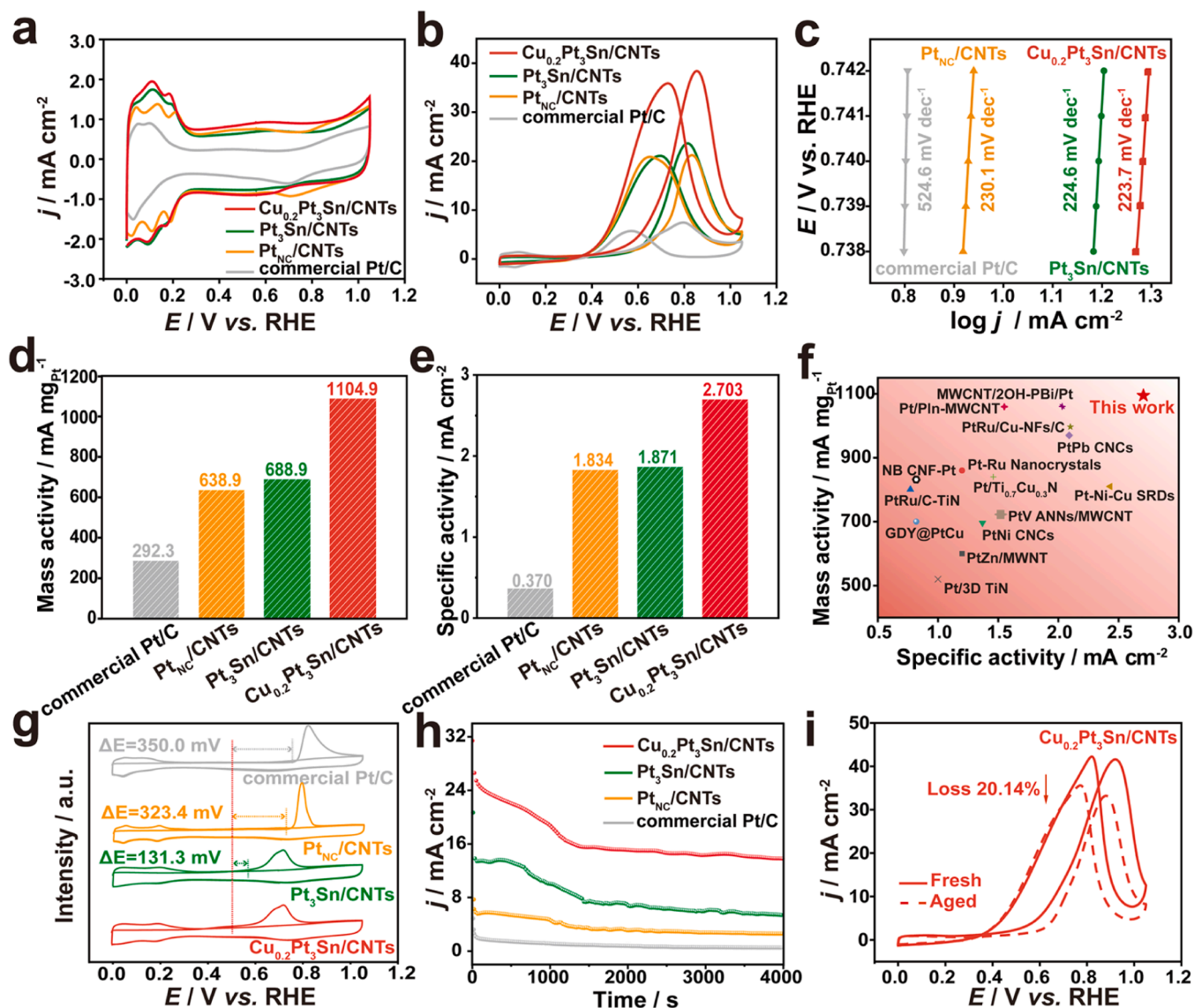
Fig. 4. (a) CVs for catalysts measured in 0.5 M H_2SO_4 solutions. (b) CVs for catalysts measured in 0.5 M H_2SO_4 + 1.0 M CH_3OH solutions. (c) Tafel plots. (d) Comparisons of mass activity for four catalysts. (e) Comparisons of specific activity for four catalysts. (f) Comparisons of MOR activities of $Cu_{0.2}Pt_3Sn$/CNTs to reported Pt-based catalysts. (g) CO stripping voltammograms for catalysts. (h) Chronoamperometric curves of tested catalysts measured at the fixed potential of 0.8 V vs. RHE for 4000 s (i) CV curves of MOR before and after 1500 cycles stability test for $Cu_{0.2}Pt_3Sn$/CNTs.

will be discussed in detail later). As listed in Table S4, the specific value of the ECSA-CO was estimated to be 40.88 m^2 g^{-1}, 36.82 m^2 g^{-1}, 34.84 m^2 g^{-1} and 78.91 m^2 g^{-1} for $Cu_{0.2}Pt_3Sn$/CNTs, Pt_3Sn/CNTs, Pt_{NC}/CNTs and commercial Pt/C, respectively, which are slightly higher than that of ECSA-H. The smaller ECSA value of $Cu_{0.2}Pt_3Sn$/CNTs, Pt_3Sn/CNTs and Pt_{NC}/CNTs as compared to commercial Pt/C is due to the larger cubic particle size.

MOR activity of above electrocatalysts was then appraised by conducting CV in 0.5 M H_2SO_4 + 1.0 M CH_3OH electrolyte. As disclosed in Fig. 4b, the $Cu_{0.2}Pt_3Sn$/CNTs exhibits much more negative onset oxidation potential and stronger current densities in the forward peak as compared with others, revealing the compositional and structural superiority of $Cu_{0.2}Pt_3Sn$/CNTs. What is worth mentioning is other synthesized ternary Cu_xPt_3Sn/CNTs catalysts with disordered alloying phase (as confirmed by Fig. S1) show inferior activities to the ordered $Cu_{0.2}Pt_3Sn$/CNTs (Fig. S11), highlighting the advantages of ordered intermetallic phase structure. While the slight superior activity of Pt_{NC}/CNTs than commercial Pt/C reflects the importance of crystal shape-control in promoting the inherent MOR activity of Pt. The Tafel slopes

were then investigated to measure the MOR kinetics of the electro-catalysts. As summarized in Fig. 4c, the $Cu_{0.2}Pt_3Sn$/CNTs exhibits the lowest Tafel slope value of 223.7 mV dec^{-1}, suggesting the most favorable MOR kinetics among tested electrocatalysts. To gain deeper insights into the activity of all catalysts, the peak current associated with MOR in the forward scan was normalized to both ECSA and the loading amount of metal Pt. As summarized in Fig. 4d, the mass activity of $Cu_{0.2}Pt_3Sn$/CNTs is 1104.9 mA mg_{Pt}^{-1}, which is 1.60, 1.73 and 3.78 times greater than that of Pt_3Sn/CNTs (688.9 mA mg_{Pt}^{-1}), Pt_{NC}/CNTs (638.9 mA mg_{Pt}^{-1}) and commercial Pt/C (292.3 mA mg_{Pt}^{-1}), respectively. Meanwhile, the specific activity based on ECSA-CO of $Cu_{0.2}Pt_3Sn$/CNTs is 2.703 mA cm^{-2} (Fig. 4e), which is 1.44, 1.47 and 7.31 times higher than those of the Pt_3Sn/CNTs (1.871 mA cm^{-2}), Pt_{NC}/CNTs (1.834 mA cm^{-2}) and commercial Pt/C (0.370 mA cm^{-2}), respectively. On the whole, the MOR electrochemical activity of Pt_3Sn/CNTs have been significantly improved after light doping of Cu, clearly demonstrating the promoting role of Cu on Pt_3Sn intermetallics for MOR. Moreover, the MOR electrocatalytic activity of $Cu_{0.2}Pt_3Sn$/CNTs is also comparable to the state-of-art PtRu/C catalysts (Fig. S12a, b), and far

more superior to many reported Pt-based catalysts in acidic electrolytes, as briefly listed in Fig. 4f and Table S5.

The anti-poisoning ability of adsorbed CO* intermediates on different catalysts was explored by CO stripping voltammetry. As depicted in Fig. 4g, the onset potential of CO oxidation for the fabricated Cu$_{0.2}$Pt$_3$Sn/CNTs is 131.3 mV, 323.4 mV and 350.0 mV lower than that of Pt$_3$Sn/CNTs, Pt$_{NC}$/CNTs and commercial Pt/C, respectively. Such an earlier onset potential suggests that CO is easier to be oxidized and removed on the surface of Cu$_{0.2}$Pt$_3$Sn/CNTs, revealing its stronger

capability of tolerance to CO poisoning. The CO-poisoning tolerance of Cu$_{0.2}$Pt$_3$Sn/CNTs is also on a par with that of commercial PtRu/C, as demonstrated in Fig. S12c. Long-term stability is another critical parameter for assessing the performance of electrocatalysts. Both chronoamperometry *I-t* tests and CV scanning tests were therefore performed to verify the long-term stability superiority of Cu$_{0.2}$Pt$_3$Sn/CNTs. Fig. 4h exhibits the *I-t* curve of tested catalysts at 0.8 V vs. RHE. It can be seen that the current density attenuates sharply at first and levels out gradually, due to the accumulation of and poisoning by the intermediate
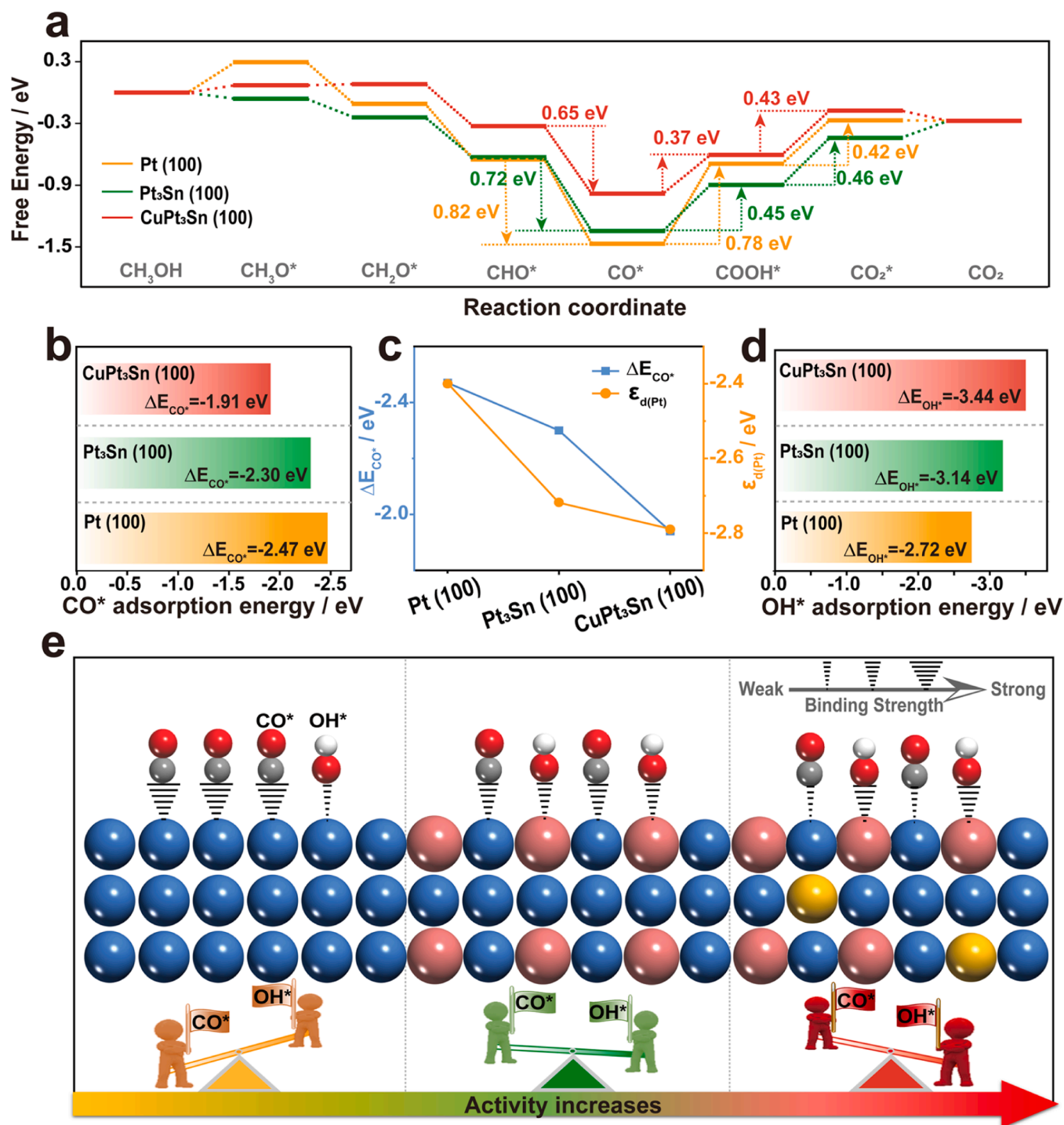

Fig. 5. (a) The free energy diagram of MOR on modeled surfaces. (b) Adsorption energy of CO* of modeled surfaces. (c) The relationship between ΔE_{CO^*} and d band center of Pt site ($\varepsilon_{d(Pt)}$) for CuPt$_3$Sn (100), Pt$_3$Sn (100) and Pt (100) model. (d) Adsorption energy of OH* of modeled surfaces. (e) Schematic illustration of ΔE_{CO^*} and ΔE_{OH^*} differences in CuPt$_3$Sn (100), Pt$_3$Sn (100) and Pt (100) models.

species on the active sites[49]. The current drop trend of $Cu_{0.2}Pt_3Sn/CNTs$ is gentler and the retained current density of $Cu_{0.2}Pt_3Sn/CNTs$ is much higher than $Pt_3Sn/CNTs$, $Pt_{NC}/CNTs$, commercial Pt/C, and as well as commercial PtRu/C (Fig. S12d). The aged $Cu_{0.2}Pt_3Sn/CNTs$ after the *I-t* test was characterized by TEM and ICP-AES, and the results well affirms the good structural and compositional stability of $Cu_{0.2}Pt_3Sn/CNTs$ (Fig. S13, Table S6). Additionally, the $Cu_{0.2}Pt_3Sn/CNTs$ only exhibits 20.14% decay after 1500 sequential CV cycles, better than that of $Pt_3Sn/CNTs$ (31.72%, Fig. S14a), $Pt_{NC}/CNTs$ (38.74%, Fig. S14b) and commercial Pt/C (50.50%, Fig. S14c) and commercial PtRu/C (41.15%, Fig. S14d), further certifying the high stability of $Cu_{0.2}Pt_3Sn/CNTs$. To sum up, above findings suggest that the slight Cu doped Pt_3Sn intermetallic catalyst exhibits a dual improvement in catalytic activity and stability, holding great promises as an effective catalyst for methanol electrooxidations.

DFT calculations were then implemented to comprehend the MOR reaction mechanism on different electrocatalysts. The full-reaction free energy diagram (Fig. 5a) for MOR on the simulated surfaces was investigated by examining the CO-poisoning pathway as follows: $CH_3OH^* \rightarrow CH_3O^* \rightarrow CH_2O^* \rightarrow CHO^* \rightarrow CO^* \rightarrow COOH^* \rightarrow CO_2^* \rightarrow CO_2$ (Fig. S15-S17). It is found that the addition of OH* on CO* to form the COOH* and the subsequent conversion of COOH* to CO_2^* require relative high free energy inputs, which are considered to be overpotential-determining steps for MOR. Be specific, the $CuPt_3Sn$ (100) only needs the energy costs of 0.37 eV and 0.43 eV for these two steps, respectively, lower than those on Pt (100) and Pt_3Sn (100) models, suggesting that the poisonous CO* can be more easily oxidized to CO_2^* on the $CuPt_3Sn$ (100). It is also noted the $CuPt_3Sn$ (100) exhibits a smaller energy releases (0.65 eV) for the CHO*→CO* step as compared to Pt_3Sn (100) (0.72 eV) and Pt (100) (0.82 eV), signifying a weaker trend to produce CO* and a lower possibility for CO* poisoning effect of the $CuPt_3Sn$ (100) surface. These results strongly validate the CO-stripping experiment.

To shed light on the differences in CO-resistance, we further calculated the absorption energy of CO* (ΔE_{CO^*}) and OH* (ΔE_{OH^*}), two pivotal descriptors for the MOR, on above-mentioned three models. As displayed in Fig. 5**b**, the ΔE_{CO^*} (−1.91 eV) at the Pt site of $CuPt_3Sn$ (100) surface is higher than that of Pt_3Sn (100) (−2.30 eV) and Pt (100) surfaces (−2.47 eV), revealing a weaker interaction between toxic CO* and $CuPt_3Sn$ (100) surface. Noting that the descending sequence of the CO* binding energy on three modelled surfaces is consistent with that of their d-band center position (Fig. 5c), well conforming to the d-band center theory. With regard to the OH* intermediate, it can stably adsorb on the top sites of the pure Pt (100) surface (Fig. S18a), with the ΔE_{OH^*} value of − 2.72 eV (Fig. 5d). While the OH* favors for bridge-bonding with both Pt and Sn atoms located on intermetallic Pt_3Sn (100) surface (Fig. S18b) with a lowered ΔE_{OH^*} as compared to the pure Pt (100), indicating a strengthened OH* adsorption. This can be due to the presence of oxyphilic Sn metals that are beneficial to adsorbing oxygen-containing species [37,38]. The Cu-doped Pt_3Sn (100) surface also inherits the bridge adsorption type of OH* that linking with both Pt and Sn atoms (Fig. S18c), but its ΔE_{OH^*} becomes slightly stronger as compared to the non-Cu doped Pt_3Sn (100) surface, indicating that the $CuPt_3Sn$ (100) binds OH* more easily, which is coincide with the XPS results. Combined with above XPS, PDOS and electrochemical results together, the diminished energy cost of CO*→ COOH* step on the $CuPt_3Sn$ (100) surface and the differences of MOR activity delivered by $Cu_{0.2}Pt_3Sn/CNTs$, $Pt_3Sn/CNTs$ and $Pt_{NC}/CNTs$ can be well explained. The light incorporation of Cu into Pt_3Sn intermetallics induces a strong 5d-5p-3d orbital hybridization and a distinct charge redistribution, which alter the electron configuration of surface Pt to be more electron enriched while surface Sn to be more electron deficient. The more electrons filled in Pt 5d orbital causes the d-band center of Pt in $Cu_{0.2}Pt_3Sn/CNTs$ more far away from the Fermi level as compared to the undoped $Pt_3Sn/CNTs$ and $Pt_{NC}/CNTs$, which intrinsically cuts down the binding strength of Pt-CO* in $Cu_{0.2}Pt_3Sn/CNTs$ (as illustrated in Fig. 5e).

Simultaneously, the surface electron-deficient Sn sites binds *OH more efficiently, further expedites the kinetics of oxidation removal of *CO. The fall of CO* binding energy on Pt sites and the rise of OH* binding energy on Sn sites collectively endow the $Cu_{0.2}Pt_3Sn/CNTs$ with an accelerated CO* oxidizing and removing rates, consequently resulting in a prominently enhanced MOR activity.

4. Conclusions

To summarize, intermetallic phase composition and crystal shape engineering strategies are integrated to construct surface-uneven $Cu_{0.2}Pt_3Sn$ ternary intermetallic nanocubes to achieve dual-optimization of ΔE_{CO^*} and ΔE_{OH^*} for MOR. Both experimental outcomes and DFT calculations corroborate that the strong Pt 5d-Sn 5p-Cu 3p orbital hybridization induced by Cu heteroatom doping elevates the local electron density of Pt and downshifts its d-band center, thereby intrinsically weakening *CO adsorption on Pt sites. Inversely, the 5d-5p–3p orbital hybridization downregulates the local electron density of Sn and stimulates the generation of more Sn (II/IV) species on surface, augmenting *OH adsorption on Sn sites and hence further accelerating the oxidative removal of *CO. The optimized binding energies of dual-intermediates uniting with the architecture superiorities of surface-uneven intermetallic nanocubes collectively contribute to significantly enhanced MOR activity and stability. This work demonstrates well-shaped ternary intermetallics are promising MOR electrocatalysts and elucidates the enhancement mechanism of ternary intermetallic catalysts via multielemental couplings.

CRediT authorship contribution statement

Yao Nie: Designing the idea and experiment, Data analysis, Writing – reviewing & editing, Funding acquisition. **Zhaohong Li:** Preparing catalysts, Helping to write original draft. **Xingqun Zheng:** Conducting theoretical calculation, Data analysis, Writing – review & editing. **Yi Wang, Linping Luo, Xuejiao Xia, Sitong Yang, Chunyan Du** and **Yihan Huang:** They helped to prepare catalysts and do the repetitive experiments. **Yi Wang:** Providing server for catalyst characterizations, providing constructive suggestions, Writing – review & editing, Funding acquisition.

Declaration of Competing Interest

The authors declare that they have no known competing financial interests or personal relationships that could have appeared to influence the work reported in this paper.

Data availability

No data was used for the research described in the article.

Acknowledgements

Appendix A. Supporting information

Supplementary data associated with this article can be found in the online version at doi:10.1016/j.apcatb.2023.123494.

References

[1] Z. Xia, X. Zhang, H. Sun, S. Wang, G. Sun, Recent advances in multi-scale design and construction of materials for direct methanol fuel cells, Nano Energy 65 (2019), 104048.

[2] J. Wang, B. Zhang, W. Guo, L. Wang, J. Chen, H. Pan, W. Sun, Toward electrocatalytic methanol oxidation reaction: longstanding debates and emerging catalysts, Adv. Mater. 35 (2023) 2211099.

[3] L. Zhang, J. Zhang, W. Tan, C. Zhong, Y. Tu, H. Song, L. Du, S. Liao, Z. Cui, Amorphous TiOx stabilized intermetallic Pt3Ti nanocatalyst for methanol oxidation reaction, Nano Lett. 23 (2023) 5187–5193.

[4] J. Zhu, L. Xia, R. Yu, R. Lu, J. Li, R. He, Y. Wu, W. Zhang, X. Hong, W. Chen, Y. Zhao, L. Zhou, L. Mai, Z. Wang, Ultrahigh stable methanol oxidation enabled by a high hydroxyl concentration on Pt clusters/MXene interfaces, J. Am. Chem. Soc. 144 (2022) 15529–15538.

[5] M. Li, Z. Zhao, W. Zhang, M. Luo, L. Tao, Y. Sun, Z. Xia, Y. Chao, K. Yin, Q. Zhang, L. Gu, W. Yang, Y. Yu, G. Lu, S. Guo, Sub-monolayer YOx/MoOx on ultrathin Pt nanowires boosts alcohol oxidation electrocatalysis, Adv. Mater. 33 (2021) 2103762.

[6] Y. Yang, F.Y. Gao, X.L. Zhang, S. Qin, L.R. Zheng, Y.H. Wang, J. Liao, Q. Yang, M. R. Gao, Suppressing electron back-donation for a highly CO-tolerant fuel cell anode catalyst via cobalt modulation, Angew. Chem. Int Ed. 61 (2022), e20220804.

[7] X. Wang, M. Xie, F. Lyu, Y.-M. Yiu, Z. Wang, J. Chen, L.-Y. Chang, Y. Xia, Q. Zhong, M. Chu, H. Yang, T. Cheng, T.-K. Sham, Q. Zhang, Bismuth oxyhydroxide-Pt inverse interface for enhanced methanol electrooxidation performance, Nano Lett. 20 (2020) 7751–7759.

[8] X. Wu, Y. Jiang, Y. Yan, X. Li, S. Luo, J. Huang, J. Li, R. Shen, D. Yang, H. Zhang, Tuning surface structure of Pd3Pb/PtnPb nanocrystals for boosting the methanol oxidation reaction, Adv. Sci. 6 (2019) 1902249.

[9] Y. Tan, Z. Zhang, Z. Lei, L. Yu, W. Wu, Z. Wang, N. Cheng, Electronic modulation optimizes OH* intermediate adsorption on Co-Nx-C sites via coupling CoNi alloy in hollow carbon nanopolyhedron toward efficient reversible oxygen electrocatalysis, Appl. Catal. B 304 (2022), 121006.

[10] L. Huang, X. Zhang, Q. Wang, Y. Han, Y. Fang, S. Dong, Shape-control of Pt–Ru nanocrystals: tuning surface structure for enhanced electrocatalytic methanol oxidation, J. Am. Chem. Soc. 140 (2018) 1142–1147.

[11] M. Qiao, F.Y. Meng, H. Wu, Y. Wei, X.F. Zeng, J.X. Wang, PtCuRu nanoflowers with Ru-rich edge for efficient fuel-cell electrocatalysis, Small 18 (2022) 2204720.

[12] C. Li, X. Chen, L. Zhang, S. Yan, A. Sharma, B. Zhao, A. Kumbhar, G. Zhou, J. Fang, Synthesis of Core@Shell Cu-Ni@Pt-Cu nano-octahedra and their improved MOR activity, Angew. Chem. Int Ed. 60 (2021) 7675–7680.

[13] S. Zhang, Z. Zeng, Q. Li, B. Huang, X. Zhang, Y. Du, C.-H. Yan, Lanthanide electronic perturbation in Pt–Ln (La, Ce, Pr and Nd) alloys for enhanced methanol oxidation reaction activity, Energy Environ. Sci. 14 (2021) 5911–5918.

[14] J.-H. Zheng, G. Li, J.-M. Zhang, N. Cheng, L.-F. Ji, J. Yang, J. Zhang, B.-W. Zhang, Y.-X. Jiang, S.-G. Sun, 15-General strategy for evaluating the d-band center shift and ethanol oxidation reaction pathway towards Pt-based electrocatalysts, Sci. China Chem. 66 (2023) 279–288.

[15] H. Cheng, J. Xia, M. Wang, C. Wang, R. Gui, X. Cao, T. Zhou, X. Zheng, W. Chu, H. Wu, Y. Xie, C. Wu, Surface anion promotes Pt electrocatalysts with high CO tolerance in fuel-cell performance, J. Am. Chem. Soc. 144 (2022) 22018–22025.

[16] J. Gao, X. Zhou, Y. Wang, Y. Chen, Z. Xu, Y. Qiu, Q. Yuan, X. Lin, H.J. Qiu, Exploiting the synergistic electronic interaction between Pt-skin wrapped intermetallic PtCo nanoparticles and Co-N-C support for efficient ORR/EOR electrocatalysis in a direct ethanol fuel cell, Small 18 (2022) 2202071.

[17] Z. Liu, G. Fu, J. Li, Z. Liu, L. Xu, D. Sun, Y. Tang, Facile synthesis based on novel carbon-supported cyanogel of structurally ordered Pd3Fe/C as electrocatalyst for formic acid oxidation, Nano Res. 11 (2018) 4686–4696.

[18] W.-J. Zeng, C. Wang, P. Yin, L. Tong, Q.-Q. Yan, M.-X. Chen, S.-L. Xu, H.-W. Liang, Alloying matters for ordering: synthesis of highly ordered PtCo intermetallic catalysts for fuel cells, Inorg. Chem. 62 (2023) 5262–5269.

[19] W. Wu, Z. Zhang, Z. Lei, X. Wang, Y. Tan, N. Cheng, X. Sun, Encapsulating Pt nanoparticles inside a derived two-dimensional metal-organic frameworks for the enhancement of catalytic activity, ACS Appl. Mater. Interfaces 12 (2020) 10359–10368.

[20] W. Zhao, B. Chi, L. Liang, P. Yang, W. Zhang, X. Ge, L. Wang, Z. Cui, S. Liao, Optimizing the electronic structure of ordered Pt–Co–Ti ternary intermetallic catalyst to boost acidic oxygen reduction, ACS Catal. 12 (2022) 7571–7578.

[21] J. Zhu, Y. Yang, L. Chen, W. Xiao, H. Liu, H.D. Abruña, D. Wang, Copper-induced formation of structurally ordered Pt–Fe–Cu ternary intermetallic electrocatalysts with tunable phase structure and improved stability, Chem. Mater. 30 (2018) 5987–5995.

[22] Y. Wang, H. Lv, L. Sun, F. Jia, B. Liu, Ordered mesoporous intermetallic trimetals for efficient and pH-universal hydrogen evolution electrocatalysis, Adv. Energy Mater. 12 (2022) 2201478.

[23] Z. Xing, J. Li, S. Wang, C. Su, H. Jin, Structure engineering of PtCu3/C catalyst from disordered to ordered intermetallic compound with heat-treatment for the methanol electrooxidation reaction, Nano Res. 15 (2021) 3866–3871.

[24] C. Jung, C. Lee, K. Bang, J. Lim, H. Lee, H.J. Ryu, E. Cho, H.M. Lee, Synthesis of chemically ordered Pt3Fe/C intermetallic electrocatalysts for oxygen reduction reaction with enhanced activity and durability via a removable carbon coating, ACS Appl. Mater. Interfaces 9 (2017) 31806–31815.

[25] Y. Nie, X. Qi, R. Wu, R. Yang, H. Wang, M. Deng, S. Zhang, S. Lu, Z. Gu, X. Liu, structurally ordered PtFe intermetallic nanocatalysts toward efficient electrocatalysis of methanol oxidation, Appl. Surf. Sci. 569 (2021), 151004.

[26] X. Zhao, H. Cheng, L. Song, L. Han, R. Zhang, G. Kwon, L. Ma, S.N. Ehrlich, A. I. Frenkel, J. Yang, K. Sasaki, H.L. Xin, Rhombohedral ordered intermetallic nanocatalyst boosts the oxygen reduction reaction, ACS Catal. 11 (2020) 184–192.

[27] Y. Xu, X. Cui, S. Wei, Q. Zhang, L. Gu, F. Meng, J. Fan, W. Zheng, Highly active zigzag-like Pt-Zn alloy nanowires with high-index facets for alcohol electrooxidation, Nano Res. 12 (2019) 1173–1179.

[28] X. Hu, Z. Xiao, W. Wang, L. Bu, Z. An, S. Liu, C.-W. Pao, C. Zhan, Z. Hu, Z. Yang, Y. Wang, X. Huang, Platinum–lead–bismuth/platinum–bismuth core/shell nanoplate achieves complete dehydrogenation pathway for direct formic acid oxidation catalysis, J. Am. Chem. Soc. 145 (2023) 15109–15117.

[29] H. Rong, J. Mao, P. Xin, D. He, Y. Chen, D. Wang, Z. Niu, Y. Wu, Y. Li, Kinetically controlling surface structure to construct defect-rich intermetallic nanocrystals: effective and stable catalysts, Adv. Mater. 28 (2016) 2540–2546.

[30] J. Zhang, W. Xu, L. Xu, Q. Shao, X. Huang, Concavity tuning of intermetallic Pd–Pb nanocubes for selective semihydrogenation catalysis, Chem. Mater. 30 (2018) 6338–6345.

[31] H. Lv, Y. Zheng, Y. Wang, J. Wang, B. Liu, Z.A. Qiao, Ordered mesoporous intermetallic Ga-Pt nanoparticles: phase-controlled synthesis and performance in oxygen reduction electrocatalysis, Angew. Chem. Int Ed. 62 (2023), e202304420.

[32] Y. Wang, M. Zheng, Y. Li, C. Ye, J. Chen, J. Ye, Q. Zhang, J. Li, X.Z. Fu, J. Wang, S.G. Sun, D. Wang, p–d orbital hybridization induced by a monodispersed Ga site on a Pt3Mn nanocatalyst boosts ethanol electrooxidation, Angew. Chem. Int. Ed. 61 (2022), e202115735.

[33] F. Kong, X. Liu, Y. Song, Z. Qian, J. Li, L. Zhang, G. Yin, J. Wang, D. Su, X. Sun, Selectively coupling Ru single atoms to PtNi concavities for high-performance methanol oxidation via d-band center regulation, Angew. Chem. Int. Ed. 61 (2022), e202115735.

[34] M. Xie, Z. Lyu, R. Chen, M. Shen, Z. Cao, Y. Xia, Pt–Co@Pt octahedral nanocrystals: enhancing their activity and durability toward oxygen reduction with an intermetallic core and an ultrathin shell, J. Am. Chem. Soc. 143 (2021) 8509–8518.

[35] Y. Chen, J. Pei, Z. Chen, A. Li, S. Ji, H. Rong, Q. Xu, T. Wang, A. Zhang, H. Tang, J. Zhu, X. Han, Z. Zhuang, G. Zhou, D. Wang, Pt atomic layers with tensile strain and rich defects boost ethanol electrooxidation, Nano Lett. 22 (2022) 7563–7571.

[36] T. Yang, F. Qin, S. Zhang, H. Rong, W. Chen, J. Zhang, Atomically dispersed Ru in Pt3Sn intermetallic alloy as an efficient methanol oxidation electrocatalyst, Chem. Comm. 57 (2021) 2164–2167.

[37] H.-S. Chen, T.M. Benedetti, J. Lian, S. Cheong, P.B. O'Mara, K.O. Sulaiman, C.H. W. Kelly, R.W.J. Scott, J.J. Gooding, R.D. Tilley, Role of the secondary metal in ordered and disordered Pt–M intermetallic nanoparticles: an example of Pt3Sn nanocubes for the electrocatalytic methanol oxidation, ACS Catal. 11 (2021) 2235–2243.

[38] L. Wang, W. Wu, Z. Lei, T. Zeng, Y. Tan, N. Cheng, X. Sun, High-performance alcohol electrooxidation on Pt3Sn–SnO2 nanocatalysts synthesized through the transformation of Pt–Sn nanoparticles, J. Mater. Chem. A 8 (2020) 592–598.

[39] Q. Wang, S. Chen, P. Li, S. Ibraheem, J. Li, J. Deng, Z. Wei, Surface Ru enriched structurally ordered intermetallic PtFe@PtRuFe core-shell nanostructure boosts methanol oxidation reaction catalysis, Appl. Catal. B 252 (2019) 120–127.

[40] X. Zou, S. Chen, Q. Wang, X. Gao, J. Li, J. Li, L. Li, W. Ding, Z. Wei, Leaching- and sintering-resistant hollow or structurally ordered intermetallic PtFe alloy catalysts for oxygen reduction reactions, Nanoscale 11 (2019) 20115–20122.

[41] X. Zhang, L. Hui, D. Yan, J. Li, X. Chen, H. Wu, Y. Li, Defect rich structure activated 3D palladium catalyst for methanol oxidation reaction, Angew. Chem. Int. Ed. 62 (2023), e2023089.

[42] H. Wang, S. Zhang, W. Cai, B.Z. Xu, Z. Cai, Y. Wu, X. Luo, X. Wei, Z. Liu, W. Gu, A. Eychmüller, C. Zhu, J. Chen, Largely boosted methanol electrooxidation using ionic liquid/PdCu aerogels via interface engineering, Mater. Horiz. 7 (2020) 2407–2413.

[43] Q. Fang, H. Wang, X. Lv, X. Wei, X. Luo, J. Huang, L. Jiao, W. Gu, W. Song, C. Zhu, Trace iridium as "adhesive" in PtCuIr aerogels for robust methanol electrooxidation, ACS Sustain. Chem. Eng. 9 (2021) 13039–13046.

[44] Y. Tang, Y. Chen, Y. Wu, W. Xu, Z. Luo, H.-R. Ye, W. Ye, W. Song, S. Guo, C. Zhu, High-indexed intermetallic Pt3Sn nanozymes with high activity and specificity for sensitive immunoassay, Nano Lett. 23 (2022) 267–275.

[45] A. Nilsson, L.G.M. Pettersson, B. Hammer, T. Bligaard, C.H. Christensen, J. K. Nørskov, The electronic structure effect in heterogeneous catalysis, Catal. Lett. 100 (2005) 111–114.

[46] W. Wu, R. Chen, S. Chen, Z. Wang, N. Cheng, Optimizing d-orbital electronic configuration via metal-metal oxide core-shell charge donation for boosting reversible oxygen electrocatalysis, Small 19 (2023), e2300621.

[47] Z. Wang, S. Chen, W. Wu, R. Chen, Y. Zhu, H. Jiang, L. Yu, N. Cheng, Tailored lattice compressive strain of Pt-skins by the L1(2)-Pt(3) M intermetallic core for highly efficient oxygen reduction, Adv. Mater. 35 (2023), e2301310.

[48] Y. Tan, W. Zhu, Z. Zhang, W. Wu, R. Chen, S. Mu, H. Lv, N. Cheng, Electronic tuning of confined sub-nanometer cobalt oxide clusters boosting oxygen catalysis and rechargeable Zn–air batteries, Nano Energy 83 (2021) 105813.

[49] M. Qiao, F.Y. Meng, H. Wu, Y. Wei, X.F. Zeng, J.X. Wang, PtCuRu nanoflowers with Ru-rich edge for efficient fuel-cell electrocatalysis, Small 18 (2022), e2204720.